ROYAL SOCIETY
OF CHEMISTRY

PAPER

Check for updates

Naturally three-dimensional laminated porous carbon network structured short nano-chains bridging nanospheres for energy storage†

Chao Wang, [ID] Ye Xiong, [ID] Hanwei Wang, [ID] Chunde Jin and Qingfeng Sun [ID] *

The electrode material is the core component of an energy storage system and determines the ultimate electrochemical performance. There is an urgent demand for carbon nanomaterials with unique structures for applications as the anode of lithium-ion batteries and supercapacitor electrodes. Here, we synthesize three-dimensional laminated porous carbon aerogels (CAs), composed of carbon nanospheres bridged with short carbon chains, by using simple annealing processes inspired by the natural structure of the kiwifruit as a precursor. The carbon material obtained at 800 °C (CA-800) exhibits a high lithium storage capacity (504.8 mA h g^{-1} at 100 mA g^{-1}) and specific capacitance (337.4 F g^{-1} in the three-electrode electrochemical configuration and 322.9 F g^{-1} in a symmetric two-electrode supercapacitor cell at a current density of 0.5 A g^{-1}). Moreover, extensible and flexible symmetric supercapacitors obtained using CA-800 display stable electrochemical performance after a folding test with different curvatures and even 10 000 cycles of a bending test. This study considers a fascinating route of producing excellent electrode materials and energy storage devices derived from inexpensive, sustainable, and available natural resources.

Introduction

The vigorous development of advanced portable electronic devices, the continued expansion of the commercial electronics market, and the revolutionary breakthrough of unpiloted electric vehicles highlight the need for high-performance electrical energy storage and delivery devices. Lithium-ion batteries (LIBs) and supercapacitors are two of the most important types of energy storage systems. Currently, LIBs are most widely used for energy storage in commercial electrical devices because of the relatively low cost and high performance.[1–3] Meanwhile, the supercapacitor, as a novel electrochemical capacitor system, can complement batteries in applications from electronics to public transportation and renewable energy storage because of the requirements of high-power output and very long cycle life, benefiting from the reversible ion adsorption at the surface of high-surface-area conductive electrodes.[4–9] Carbon-based materials have attracted a great deal of attention for application in both LIBs and supercapacitors because of their high electrical conductivity, good chemical stability, and environmental friendliness.[10–12] As a result, a large variety of promising carbon materials have been explored for application in LIBs and supercapacitors, such as template carbon,[13–15] carbon nanotubes,[16–19] and graphene,[20–25] because of their unique structures.

However, their relatively high cost and the difficulty in adapting to large-scale industrial production have hindered their application. Commercially available activated carbon (AC), a low-cost classical porous material, has been widely used for supercapacitor electrodes, but its future is limited by the uncontrollable pore structure and inferior conductivity. For LIBs, the low charge storage capability (theoretically 372 mA h g^{-1}) of commercial graphite does not meet the requirements of high-energy and high-power devices.[26] Therefore, there is a prodigious need for low-cost carbon materials with an excellent structure for use in high-performance energy storage.

Biomass-derived carbon materials can possibly address the issue, because, compared with traditional raw carbon materials such as coal, pitch and phenolic resins, they possess the advantages of being inexpensive and environmentally friendly.[27] Accordingly, various biomasses (such as lignin,[28] loofah sponge,[29] silk,[30] ginkgo leaves,[31] shaddock peel,[32] seaweed[33] and so on) have been used as precursors to synthesize excellent carbon-based materials. Nevertheless, most efforts have depended on an additional chemical agent to obtain the unique structure, resulting in the biomass only serving as a carbon resource, and they lack commercial attraction. Biological organisms, which are typical biomasses that stem from the elaborate "design" of nature, are a brilliant carbon source for the synthesis of valuable carbon materials because they are available in high quality and are widespread; moreover, biological organisms inherently possess numerous miraculous structures, such as the close-knit multilayer cell wall structure. Additionally, the structure of a material is crucial for the

School of Engineering, Zhejiang A&F University, Hangzhou 311300, China. E-mail: qfsun@zafu.edu.cn

† Electronic supplementary information (ESI) available. See DOI: 10.1039/c7ta04178k

This journal is © The Royal Society of Chemistry 2017

J. Mater. Chem. A, 2017, 5, 15759–15770 | 15759

ultimate electrochemical performance.[34] Therefore, the dual utilization (chemical compounds and natural microstructure) of biomasses could be promising for the future of excellent low-cost carbon materials. Furthermore, as a sustainable and renewable material, biomass can be directly transformed into carbonaceous materials through simple heat treatment processes,[35,36] and this is exciting information with respect to industrial applications.

Herein, we present the preservation of the natural structure of a biomass by using successively optimized low-temperature hydrothermal and high-temperature annealing processes without any additional chemical agent. Utilizing kiwifruit as the precursor, we successfully prepared three-dimensional (3D) porous electro-conductive carbon aerogels (CAs) consisting of nanospheres, constructed from laminated single-layered carbon sheets, bridged together with short nano-chains. The obtained CAs all show well-defined micro- to mesoporous distributions, as determined by three gases (N_2, Ar, and CO_2) in sorption experiments. A good balance between porosity and graphitization (controlled by the carbonization temperature) yields a favorable electrode material. The electrode obtained using the CA carbonized at 800 °C (CA-800) delivers a high lithium storage capacity (504.8 mA h g^{-1} at 100 mA g^{-1}) and specific capacitance (337.4 F g^{-1} in the three-electrode electrochemical configuration and 322.9 F g^{-1} in a symmetric two-electrode supercapacitor cell at a current density of 0.5 A g^{-1}). Furthermore, we engineered and fabricated an extensible and flexible supercapacitor for wearable devices using CA-800, and its electrochemical performance remained nearly stable during two mechanical deformation tests.

Results and discussion

Formation of porous CAs from laminated sheet network-structured carbon spheres bridged with short carbon chains

Sponge-like carbonaceous aerogels (CAAs) were prepared by a simple one-pot hydrothermal process using the soft tissue biomass of kiwifruit. The obtained carbonaceous hydrogel has a well-defined shape (Fig. S1a†). Then, the water absorbed in the hydrogel was removed by freeze-drying to prepare the CAA, which retained the original shape well. Meanwhile, the color of the samples clearly turned from black to brown after the drying process (Fig. S1b†). To obtain porous conductive CAs, calcination in a nitrogen atmosphere is a simple and straightforward method. The thermal gravimetric (TG) curve of the CAA (Fig. 1) obtained in a nitrogen atmosphere shows a plateau at temperatures over 600 °C. Therefore, heating temperatures of 600 °C, 800 °C, and 1000 °C were chosen and correspond to the samples CA-600, CA-800, and CA-1000, respectively (Fig. S1d†). The TG curves of the obtained CAs agree with the plateau observed during the annealing of the CAAs (Fig. S1c†).

Characterization of the CAAs

The unique morphology of the CAAs inherited from the natural structure of kiwifruit is shown in the scanning electron microscopy (SEM) and transmission electron microscopy (TEM)
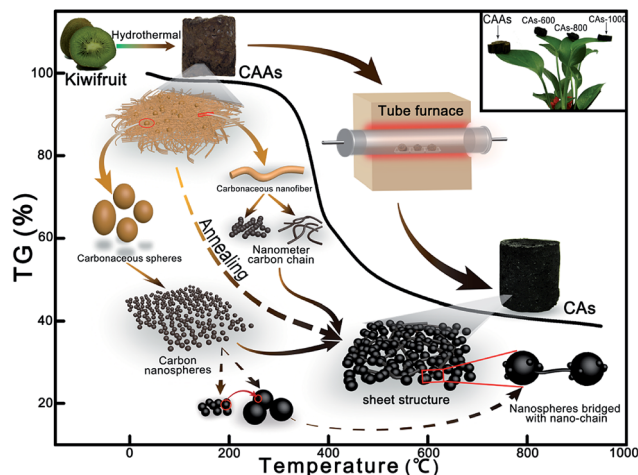

Fig. 1 TGA curves showing the schematic illustration of preparing CAs from pre-synthesized CAAs The inset shows the photograph of the CAAs and the CAs carbonized at 600 °C (CA-600), 800 °C (CA-800), and 1000 °C (CA-1000) on the leaves.

images. Fig. 2a clearly shows that the numerous carbonaceous nanospheres and abundant dense nanofibers interconnect, forming several pores in the CAAs. These nanospheres in the CAAs were produced by hydrothermally carbonizing and polymerizing the carbohydrates, and the nanofibers were mainly derived from the original fibers of kiwifruit tissues.[36,37] The TEM image (Fig. 2b) further shows that the crosslinked nanofibers have different sizes ranging from a dozen to several hundred nanometers. In the crosslinked network, it is interesting that the nanospheres are bridged by several nanofibers. The HR-TEM images (Fig. S2†) reveal the amorphous structure on the surface of the carbonaceous nanospheres. The nitrogen sorption isotherms and pore-size distribution further describe the porous properties of the CAAs (Fig. 2c), revealing the plentiful existence of mesopores approximately 3 nm in diameter.
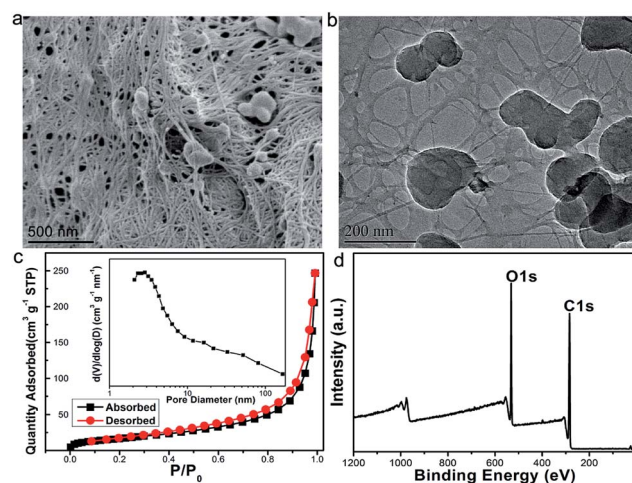

Fig. 2 Microstructure, porosity and chemical composition study of CAAs. (a) SEM images, (b) TEM images, (c) nitrogen sorption isotherms and pore size distribution, and (d) XPS survey scan spectra of the CAAs.

15760 | J. Mater. Chem. A, 2017, 5, 15759–15770

This journal is © The Royal Society of Chemistry 2017

The X-ray photoelectron spectroscopy (XPS) survey scan (Fig. 2d) indicates that the CAAs are predominantly composed of C and O elements, corresponding to the photoelectron lines at binding energies of approximately 285 and 711 eV, attributed to C 1s and O 1s, respectively. The deconvoluted C 1s core-level spectrum (Fig. S3†) contains four different signals at 283.3, 285.2, 286.8 and 288.9 eV, and they are attributed to graphitic/aliphatic carbon groups (C–C); alcohol, phenol or ether groups (C–O); carbonyl or quinone groups (C=O); and carboxylic groups, esters or lactones (–COOR), respectively. The analysis of the Fourier transform infrared (FTIR) spectra (Fig. S4†) further deduces the existence of several functional groups (*e.g.*, hydroxyl, carbonyl, carboxyl, aromatic and so on) on the surface (the detailed analysis is presented in ESI note 1†). The results illustrate the existence of multiple oxygen functional groups and a high C/O ratio (approximately 3) on the surface of the CAA. The abundance of oxygen functional groups could be due to the incomplete carbonization of the carbohydrates (glucose and sucrose) under the low-temperature (<300 °C) hydrothermal conditions. The analyses of the microstructure, porosity and chemical constitution suggest that the CAAs, derived from an environmentally friendly renewable biomass, are qualified precursors for the synthesis of valuable carbon materials, for which a porous structure and an abundance of high-quality carbon content are required.

Characterization of CAs

The high-temperature annealing process is a straightforward and powerful procedure for the fabrication of quality carbon materials. After calcination in a nitrogen atmosphere, the microstructures of the samples were obtained using SEM and TEM. Rough sheets constitute the 3D porous microstructure architectures of these CAs (Fig. 3a–c). Zooming in on the rough surfaces (Fig. S5a–c†) reveals that the porous sheets consist of carbon nanospheres with papillae and nanometer carbon catenulate networks. TEM images (Fig. 3d–f) further clearly present the junction between the carbon nanospheres and nanometer carbon chains. We find that these short carbon nano-chains gradually transform into a bead-like structure and even break with increasing calcination temperature. As shown in Fig. S5d–f,† the high-resolution TEM (HR-TEM) images exhibit lattice fringes that are increasingly clear with increased heat-treatment temperature; this is also illustrated by the corresponding diffraction patterns. The results provide direct evidence that a higher annealing temperature generates greater graphitization. The elemental mappings (Fig. S5g–i†) of the three CAs
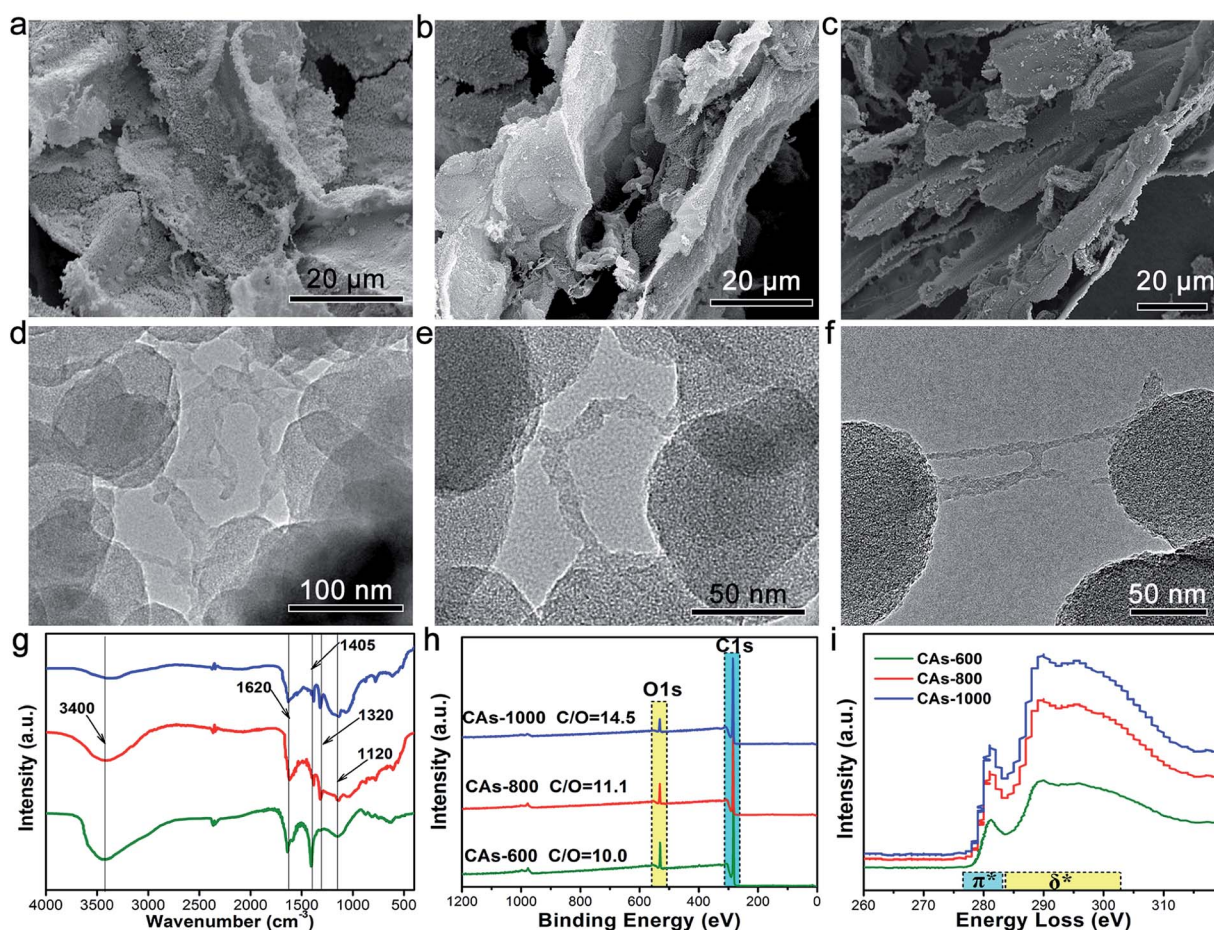

Fig. 3 Microstructure and chemical composition study of CA-600, CA-800 and CA-1000. (a–c) SEM images of CA-600, CA-800 and CA-1000. (d–f) TEM images of CA-600, CA-800 and CA-1000. (g) FTIR spectra, (h) XPS survey scan spectra and (i) EELS spectra of CA-600, CA-800 and CA-1000.

indicate that the carbon element has a wider distribution than the oxygen element, which can be attributed to the greater surface graphitization in these nanometer components. Carbon spheres (named RFCS-600) derived from a monodisperse resorcinol-formaldehyde resin polymer were fabricated for comparison,[38] and their SEM image is shown in Fig. S6.†

To investigate the influence of the annealing temperature on the chemical composition of the samples, FTIR spectroscopy and XPS were conducted to compare CA-600, CA-800 and CA-1000. As shown in Fig. 3g, all samples present similar FTIR spectra: a broad absorption band centered approximately at 3400 cm^{-1} is attributed to the O–H stretching vibration of adsorbed water molecules; the strong absorption band centered at 1620 cm^{-1} is ascribed to C=C stretching vibrations; the relatively weak band centered at 1405 cm^{-1} is attributed to C–C stretching vibrations; and the relatively broad band centered approximately at 1120 cm^{-1} could result from C–O stretching vibrations. Further measurements were also made using XPS,

and the comparison of the three survey scans reveals that the intensity of the O 1s clearly decreases with increase in the temperature, in agreement with the augmentation of the C/O atomic ratio (Fig. 3h). Furthermore, the C 1s spectra (Fig. S7†) reveal that the amount of sp^2-bonding increases with the annealing temperature. The quantification of the amount of sp^2-bonding can be conducted by measuring the ratio of π* bonding to π* + δ* bonding using electron energy loss spectroscopy (EELS). A comparison of the carbon K near-edge structure for CAs of similar thickness is shown in Fig. 3g. With the assumption that the sp^2-bonding in CA-1000 is 1, CA-600 and CA-800 were determined to have sp^2-bonding of 0.53 and 0.92.

The characterization of the CAs by means of synchrotron powder X-ray diffraction (XRD) and Raman spectroscopy is shown in Fig. 4a and d. A comparison with CA-600 indicates that the (002) peaks of CA-800 and CA-1000 have a well-developed intensity and are markedly broadened, while the peaks
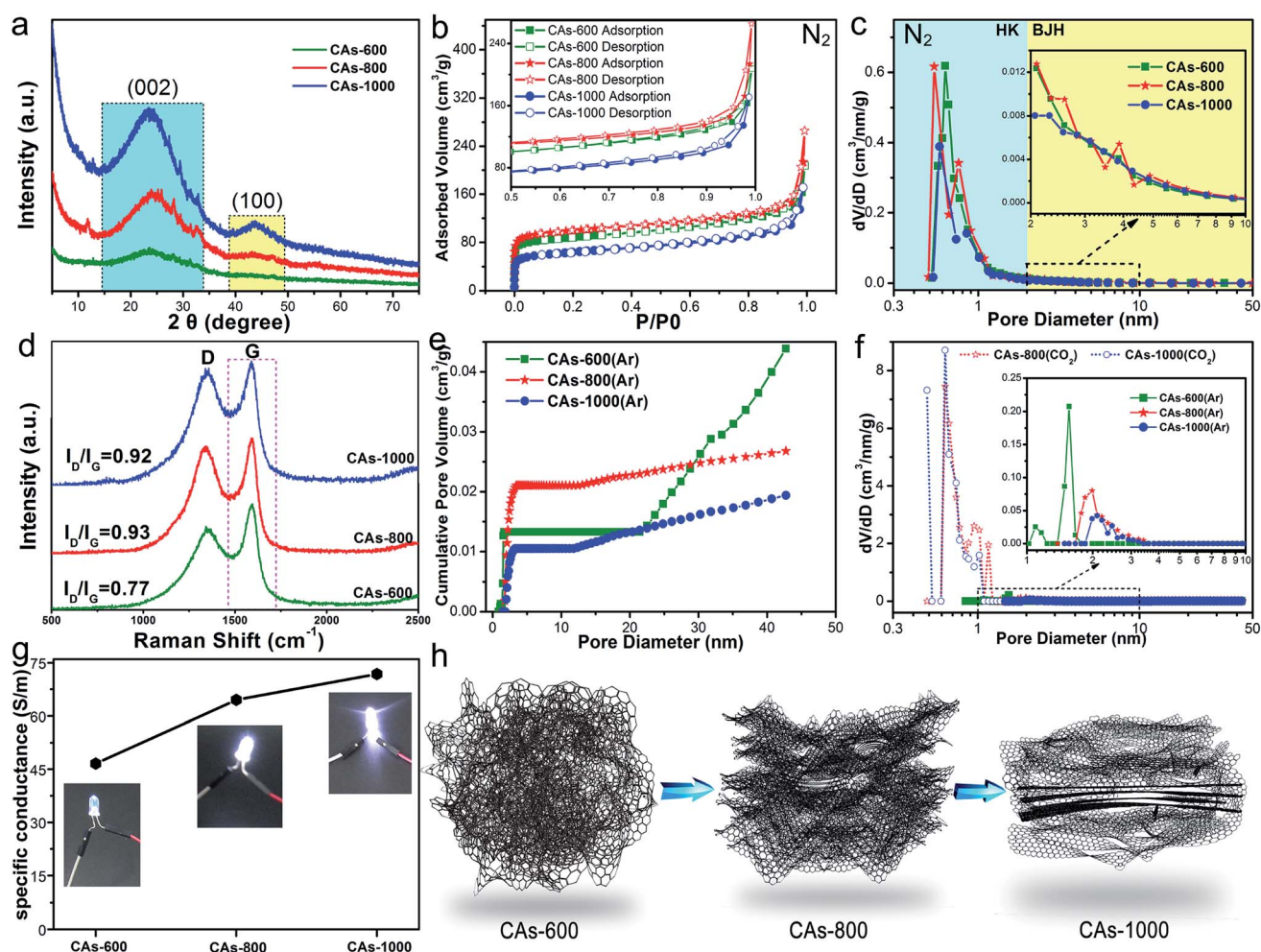

Fig. 4 (a) XRD patterns of CA-600, CA-800 and CA-1000. (b) N$_2$ adsorption–desorption isotherms of heat treated CAs at different temperatures. All exhibit typical Langmuir hysteresis corresponding to the presence of mesopores. (c) Pore size distribution of CA-600, CA-800 and CA-1000 for N$_2$ (calculated by the BJH method for mesopores and HK method for macropores). (d) Raman spectra comparison of the three CAs. (e) Cumulative pore volume of CA-600, CA-800 and CA-1000 for Ar (calculated by using NLDFT). (f) Pore-size distribution of CA-600, CA-800 and CA-1000 for Ar and CO$_2$ (calculated by using the NLDFT model). (g) Conductivities of CA-600, CA-800 and CA-1000. The insets show the digital photos of LED bulb using these CAs as conductor under the same power supply. (h) Sketches of the graphitization process.

15762 | J. Mater. Chem. A, 2017, 5, 15759–15770

This journal is © The Royal Society of Chemistry 2017

centered at 44.8° (100) have an interesting increased intensity. The results are consistent with the observations from HR-TEM, which indicate that the graphitic stacking and intra-layer condensation occur after annealing.[40] A large increase in the low-angle scattering in CA-800 and CA-1000 is also noted, which is consistent with the presence of a high density of pores.[39] Raman spectroscopy (Fig. 4d) further illustrates the improvement in graphitization. The peaks located at approximately 1320 and 1590 cm^{-1} are ascribed to the characteristic D (defects and disorder) and G (graphitic) bands of carbon materials, respectively.[41] The intensity ratio of the D and G peaks indicates the degree of structural order with respect to a perfect graphitic structure. Compared with that of CA-600, the ratio (D/G) of CA-800 is evidently increased, revealing that defect structures are increasingly generated with elevating carbonization temperature, probably related to more armchair edges of graphite. CA-1000 has a similar D/G (0.92), indicating no clear increase in graphitization. Improvement in electrical conductivity can be expected with increasing the annealing temperature. The specific conductance values of CA-600, CA-800 and CA-1000 are 46.6, 64.5 and 71.8 S m^{-1}, respectively, and this is also reflected by the luminance of a bulb with the same power supply (Fig. 4g).

That the CAs possess abundant nanometer pore canals was confirmed by electron microscopy. Further pore characterizations of these samples were performed by coupling high-resolution N_2, Ar and CO_2 adsorption/desorption experiments. The N_2 adsorption/desorption isotherms, as shown in Fig. 4b, are of the type-IV curves with the hysteresis loops (according to IUPAC classification)[42] resulting from the capillary constrictions in mesoporous structures, as well as the nearly vertical plots of the low-pressure regions attributed to micropore filling. The result indicates the coexistence of both micropore and mesopore structures in these materials; therefore, the pore size distributions should be evaluated by both the Horvath–Kawazoe (HK) model for micropores and the Barrett–Joyner–Halenda (BJH) method for mesopores. In the middle–high pressure region, the inset in Fig. 4b shows type H4 hysteresis loops for CA-800 and CA-1000 and type H1 loop for CA-600 (according to IUPAC classifications).[42] This result is also supported by the argon sorption experiment (Fig. S8†) and is indicative of the more plate-like structure in CA-800 and CA-1000 compared with that of CA-600. The pore size distributions obtained by the HK and BJH methods are displayed in Fig. 4c. The most prominent pores are in the micropore region for all three carbon materials, and this result is in good agreement with the porosity data summarized in Table 1. It is evident that the surface area and pore volume increase as the annealing temperature increases

from 600 to 800 °C. However, as the temperature rises to 1000 °C, the surface area and pore volume are distinctly reduced, likely because of the collapse of pores and an enhanced orientation during the carbonization process. Within this context, advanced methods based on density functional theory (DFT) were used for analyzing the pore volume and size. Fig. 4e shows a comparison of the cumulative pore volumes from the Ar adsorption experiment obtained by utilizing a nonlocal DFT (NLDFT) method. Containing pores with widths not exceeding approximately 3 nm, CA-800 exhibits the highest cumulative pore volume. In addition, CO_2 adsorption was performed to assess ultramicropores (pores of width < 0.7 nm). The pore size analyses from Ar and CO_2 adsorptions *via* applying a NLDFT method are revealed in Fig. 4f (the CO_2 adsorption experiment failed to measure ultramicropores in CA-600). CA-1000 only has a well-defined peak at approximately 0.65 nm for the CO_2 adsorption experiment, and CA-800 shows a broader pore size distribution, in which there is a prominent peak at approximately 0.65 nm and distinctive shoulder peaks at approximately 0.9 nm and 1.1 nm. The pore characterization analysis indicates the existence of well-defined micropores and mesopores in these carbon materials. Additionally, a schematic of the changes in carbon configuration with temperature is presented in Fig. 4h. The rational pore distribution can provide a favorable path for the transportation and penetration of electrolyte ions. Therefore, these CAs derived from kiwifruit could be promising electrode materials for energy storage, especially in the application of LIBs and supercapacitors.

Electrochemical properties for LIBs

To evaluate CAs as the anode material for LIBs, assembled half-cells with a metallic Li counter electrode were examined using cyclic voltammetry (CV) and galvanostatic cycling techniques. Fig. 5a shows the compared charge–discharge profiles of these CAs and RFCS-600 after the first and second cycles at a current density of 100 mA g^{-1} in a voltage range of 0.01–3.0 V (*vs.* Li^+/Li). RFCS-600, CA-600, CA-800, and CA-1000 deliver initial discharge capacities of 743.9, 866.5, 904.9, and 648.5 mA h g^{-1}, respectively, and the corresponding charge capacities are evidently lower. The irreversible results can be ascribed to the formation of solid-electrolyte-interphase (SEI) layers,[43] which are inferred from the CV measurements (Fig. S9†). The SEI layers covering the surface of the nanomaterials prevent further reaction between the components of the electrolyte and the active materials.[44] In the second cycle, their reversible discharge capacities are 361.6, 470.1, 504.8, and 314.4 mA h g^{-1} with capacity retentions of 48.9, 54.2, 55.8, and 63.9%, respectively.

Table 1 Pore characteristics of CA-600, CA-800, and CA-1000

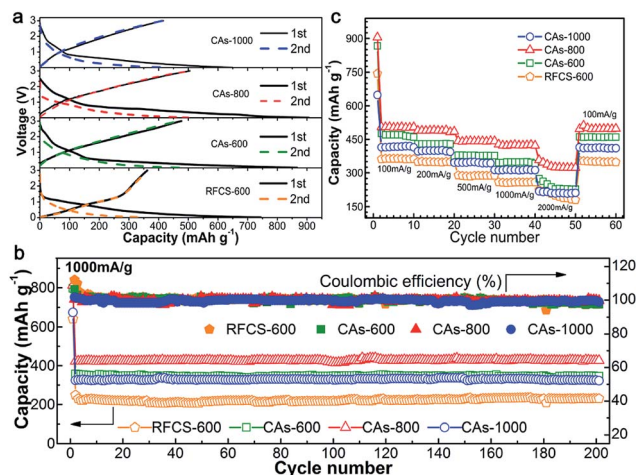| Samples	S_{BET} (m^2 g^{-1})	S_{micro} (m^2 g^{-1})	S_{meso} (m^2 g^{-1})	$S_{Langmuir}$ (m^2 g^{-1})	V_{pore}^a (cm^3 g^{-1})	V_{micro}^a (cm^3 g^{-1})	V_{meso}^a (cm^3 g^{-1})	D_{aver}^a (nm)
CA-600	332.6	247.4	85.2	416.1	0.32	0.10	0.22	4.3
CA-800	379.0	304.9	74.0	461.9	0.41	0.15	0.26	3.8
CA-1000	237.5	165.5	72.0	305.3	0.26	0.09	0.17	4.4

[a] Obtained by the BJH method.

This journal is © The Royal Society of Chemistry 2017

J. Mater. Chem. A, 2017, **5**, 15759–15770 | **15763**

Fig. 5 Electrochemical characterization for anodes of LIBs. (a) The first and second charge and discharge profiles at 100 mA g^{-1}. (b) The comparison of cycling performance. (c) Rate performance from 100 to 2000 mA g^{-1}.

The results indicate that these CAs all possess a deintercalation capacity, and CA-800 displays the highest reversible capacity.

Fig. 5b compares the cycle performance over 200 cycles of RFCS-600, CA-600, CA-800, and CA-1000 under identical conditions (1000 mA g^{-1}). CA-800 shows the highest reversible capacity and excellent cycling performance (426.1 mA h g^{-1} after 200 cycles), and its coulombic efficiency remains stable (99.4%) under the cycle tests. CA-600 and CA-1000 present inferior capacities of 345.2 and 329.8 mA h g^{-1}, respectively, but their coulombic efficiencies are similar to CA-800. The results indicate that the laminated carbon structure composed of short nano-chains bridging nanospheres can maintain the structural integrity of the electrode during cycling. In contrast, RFCS-600 (without the bridging carbon chain) exhibits a rapid fading in capacity, especially at the beginning, which is likely associated with irreversible side reactions resulting from structural rupture and the reformation of SEI layers during cycling.[45] As expected, the RFCS-600 electrode material showed the lowest

capacity. Moreover, the rate performance of these electrodes is exhibited in Fig. 5c. The capacity retentions of all samples decrease with increasing current density from 100 to 2000 mA g^{-1}, but the capacities nearly recover their original values when the current density is restored to 50 mA g^{-1}. CA-800 can be reversibly charged to 322.4 mA h g^{-1}, even at a high current rate of 2000 mA g^{-1}, which is superior to the other samples (182.6 mA h g^{-1} for RFCS-600, 227.9 mA h g^{-1} for CA-600, and 210.8 mA h g^{-1} for CA-1000). The finding also reveals the good charge transfer kinetics and stable structural integrity of CA-800. Furthermore, Table 2 compares the performance of CA-800 with those of other state-of-art biomass-derived carbon materials as the anode of an LIB. We find that CA-800 is distinctly superior to these biomass-derived carbon materials without a chemical activation agent, and even surpasses the samples obtained with KOH activation (such as wheat stalk-derived carbon nanosheets and human hair-derived porous carbon materials). The results reveal that the 3D laminated porous carbon network structured short nano-chains bridging nanospheres improve the storage of lithium ions. Among these carbon aerogels, CA-800 presents the highest surface area with abundant micropores which could bring about the most sufficient interface between the electrode and electrolyte resulting in the largest absorption quantity of Li-ions and encourage the charge-transfer reaction.[46] Besides, a larger number of defects and vacancies of CA-800 ($I_D/I_G = 0.93$) and the relatively good electrical conductivity (64.5 S m^{-2}) can lead to the higher electrochemical reactivity and provide more active positions of Li-ion storage. For these reasons, CA-800 with the 3D laminated porous carbon network structure delivers the most favorable capacity and rate ability for LIBs.
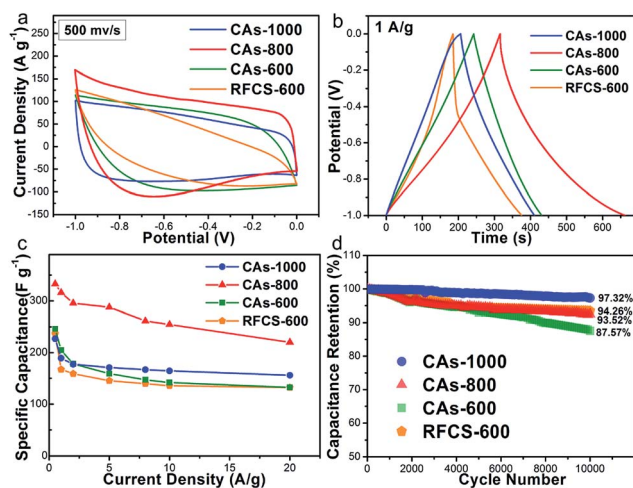
Electrochemical properties for supercapacitors

The performance of these CAs and RFCS-600 as supercapacitor electrodes in aqueous electrolytes was determined in the three-electrode electrochemical configuration in a 6 M KOH electrolyte using a Hg/HgO reference electrode and a platinum counter electrode. With CV at 500 mV s^{-1} (Fig. 6a), these CA electrodes exhibit nearly rectangular CV curves without distinct peaks in

Table 2 Comparison of the results in this work with previously reported electrochemical properties of biomass-derived carbon materials for LIB anodes[a]

Sample	Precursor	Discharge capacitance (mA h g^{-1})	Ref.
CNP	Coconut oil	464 at 0.1 A g^{-1} (20 cycles)	47
ACSB	Shell of broad beans (with KOH)	261.5 at 1 C (100 cycles)	48
OHC	Ox horns (with KOH)	304 at 5 A g^{-1}	49
PSDHC-600	Peanut shells (without any activation agent)	314 at 1 A g^{-1}	50
1100CSTs	Portobello mushroom (with KOH)	260.1 at 0.1 C	51
HGCNS	Wheat stalk (with KOH)	502 at 0.1 C	52
HHC	Human hair (with KOH)	350 at 0.3 A g^{-1}	53
BDC	Bean dreg (without any activation agent)	423 at 0.1 C	54
CA-800	Kiwifruit (without any activation agent)	504.8 at 0.1 A g^{-1} (2 cycles)	This work

[a] CNP, carbon nanoparticles; ACSB, chemically activated and carbonizing shell of broad beans; OHC, ox horn derived carbon; PSDHC-600, peanut shells derived porous hard carbons at 600 °C; CST, carbons derived from portobello mushroom cap skin tissue; HGCNS, interconnected highly graphitic carbon nanosheets; HHC, human hair derived carbon; BDC, bean dreg derived carbon.

Fig. 6 Electrochemical characterization for supercapacitors. (a) Cyclic voltammetry profiles of RFCS-600, CA-600, CA-800, and CA-1000 at 500 mV s^{-1} scan rates. (b) Charge/discharge curves of RFCS-600, CA-600, CA-800 and CA-1000 as electrodes at 1 A g^{-1} current densities. (c) Comparison of specific capacitances calculated from the discharge at different scan rates (0.5–20 A g^{-1}). (d) The cycle life of the electrodes was determined by measuring galvanostatic charge/discharge at a current density of 5 A g^{-1} for 10 000 cycles.

the -1 V to 0 V window, which indicates that the current response was primarily a result of electrical double layer (EDL) formation without contribution from a pseudo-capacitive behavior at the interface between the electrode material and electrolyte ions. In contrast, the CV curve of the RFCS-600 sample presents a shuttle shape under a similar current density, reflecting the advantage of the dual-carbon interconnected structure. Among the materials, CA-800 exhibits the highest CV performance, indicating that CA-800 is the most promising electrode material for use in a supercapacitor. The lower effective specific surface areas and pore volumes of CA-600 and CA-1000 lead to an inferior CV character. The CV curves obtained for CA materials at scan rates ranging from 10 mV s^{-1} to 2000 mV s^{-1} are plotted in Fig. S10.† The nearly rectangular CV curves of CA-800 at a high scan rate of 2000 mV s^{-1} and the nearly triangular charge/discharge curves at a high current density of 20 A g^{-1} (Fig. S10b and e†) identify a nearly ideal EDL capacitive behavior and efficient electrolyte ion transport throughout the interconnected carbon nanostructured electrode.

A comparison of the galvanostatic charge/discharge tests for the samples at 1 A g^{-1} (Fig. 6b) shows symmetric features with a fairly linear slope, and these discharges have an ignorable internal resistance (IR) drop. Consistent with the CV results, CA-800 has the longest discharge time corresponding to the highest capacitance compared with the other samples. The specific capacitances based on the active materials of working electrodes were calculated from the discharge curves at different current densities and are summarized and compared in Fig. 6c. CA-800 showed an interesting gravimetric capacitance of 337.4 F g^{-1} at a current density of 0.5 A g^{-1} and retains ~65% (219.2 F g^{-1}) of its initial capacitance as the current density increases up

to 20 A g^{-1}. In contrast, CA-600 has an inferior gravimetric capacitance of 245.9 F g^{-1} at a current density of 0.5 A g^{-1} and the lowest capacitance retention of ~53% (130.4 F g^{-1}) at 20 A g^{-1}, likely due to more heteroatoms. CA-1000 shows the greatest capacitance retention of ~68% (156.0 F g^{-1}), resulting from fewer heteroatoms and better electrical conductivity to promote its rate capability. RFCS-600 also shows a stable capacitance output at a high current density, likely because of the uniformity of its carbon sphere structure, but the specific capacity is slightly inferior to that of CA-600. The results of electrochemical impedance spectroscopy (EIS) indicate a high rate capability, low charge transfer resistance, and efficient electrolyte diffusion inside the CA-800 electrode (a detailed analysis is given in ESI note 2†). In addition, we further evaluated the suitability of the CA electrodes for practical applications, starting with their stability in sustained and cyclic loadings (Fig. 6d). After withstanding 10 000 charge/discharge cycles at a current of 5 A g^{-1}, all the retentions are ≥87.57% of their initial gravimetric capacitance, suggesting excellent cycling stability.

These electrochemical performance analyses suggest that CA-800 is the most promising electrode material for fabricating supercapacitors because of the highest specific capacitance and relatively low charge transfer resistance among the three CAs. The higher specific capacitance of CA-800 is mainly attributed to the excellent porous structure (including the higher SSA and pore volume, and well-defined pore size), which provides larger charge storage space and a smooth and convenient ion transfer pathway. In addition, the high graphitization and carbon content of CA-800 are also important for a good cycle life due to the improvement in the electric conductivity and chemical stability. More importantly, the favorable multiple synergistic effect of the unique laminated 3D networks with a bicontinuous structure, higher SSA, applicable graphitization, and oxygen-functionalization in CA-800 can accelerate extraordinary improvement in electrochemical performance for supercapacitors. Significantly, CA-800 is even superior to the carbon materials obtained by the pyrolysis of biomass with an additional chemical activation agent (such as bamboo-derived carbon, shell of broad beans-derived carbon, potato-derived carbon, and rice husk-derived carbon) but is slightly inferior to gelatin/boric-acid-derived carbon nanosheets, as shown in Table 3, further indicating that the carbon material obtained in this work is a promising electrode material for fabricating supercapacitors.

In the two-electrode system, CA-800 shows similar performance to that of the three-electrode configuration (detailed description in ESI note 3†). Moreover, we engineered and assembled extensible and flexible symmetric supercapacitors (Fig. 7a) for wearable portable devices using CA-800 as the active material, conductive copper foil as the current collector, and BMIM BF$_4$ as the electrolyte. Two mechanical deformations were performed to evaluate the potential of the supercapacitors for flexible energy storage. First, CV measurements of the CA-800 flexible supercapacitor were performed under different curvatures of the folding test (schematic displayed in the inset of Fig. 7b), and the obtained curves show nearly the same rectangular shape (Fig. 7b). The results demonstrate that the

This journal is © The Royal Society of Chemistry 2017

J. Mater. Chem. A, 2017, **5**, 15759–15770 | **15765**

Table 3 Comparison of the results in this work with previously reported electrochemical properties of biomass-derived carbon materials for supercapacitors[a]

Sample	Precursor	Electrolyte	Specific capacitance ($F\ g^{-1}$)	Ref.
BHNC	Bamboo-based industrial byproduct (with KOH)	6 M KOH	301 at 0.1 A g^{-1}	55
ACSB	Shell of broad beans (with KOH)	6 M KOH	202 at 0.5 A g^{-1}	48
N-PCs-700	Potato waste residue (with $ZnCl_2$)	2 M KOH	255 at 0.5 A g^{-1}	56
NBKBC	Bamboo (with KOH)	1 M KOH	218 at 0.2 A g^{-1}	57
CHHPCs	Corn husk (with KOH)	6 M KOH	356 at 1 A g^{-1}	58
RHPC	Rice husk ash (with hydrofluoric acid)	6 M KOH	260 at 1 A g^{-1}	59
B/N-CSs	Gelatin (with boric acid)	1 M H_2SO_4	358 at 0.1 A g^{-1}	60
PC 5-1	Pine cone (with KOH)	1 M H_2SO_4	282 at 10 mV s^{-1}	61
CA-800	Kiwifruit (without any chemical agent)	6 M KOH	337.4 at 0.5 A g^{-1}	This work

[a] BHNC, beehive-like hierarchical nanoporous carbon; ACSB, chemically activated and carbonizing shell of broad beans; N-PCs-700, nitrogen-doped porous carbon obtained at 700 °C; NBKBC, boron and nitrogen co-doped KOH-activated bamboo-derived carbon; CHHPCs, corn husk derived hierarchical porous carbons; RHPC, rice husk porous carbon; B/N-CSs, boron and nitrogen co-doped carbon nanosheets; PC 5-1, potassium hydroxide (KOH) at KOH: pine cone-derived carbon mass ratios = 5 : 1.
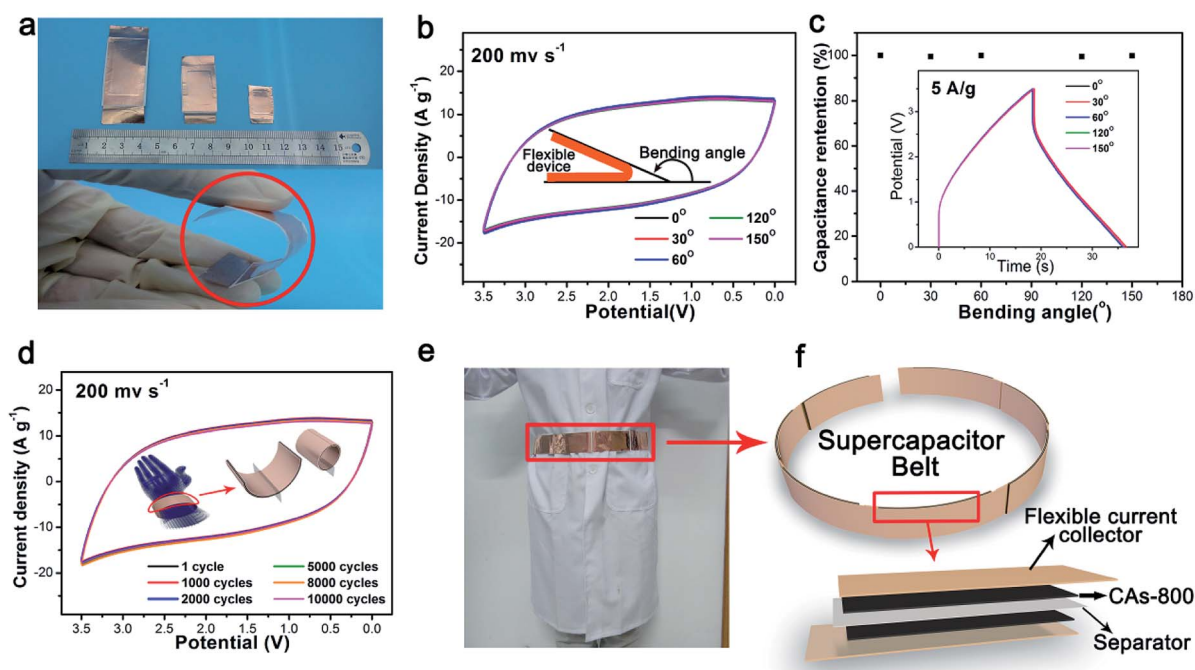
Fig. 7 Electrochemical study of flexible supercapacitors obtained using CA-800. (a) Photographs of different size and bent flexible supercapacitor devices. (b) CV curves collected at a scan rate of 200 mV s^{-1} under different folding angles. The inset shows the device under stress defining the bending angles. (c) Capacitance output stability of the devices under different bending angles. The inset shows galvanostatic charge/discharge curves at current density of 5 A g^{-1} for different bending angles. (d) CV curves at a scan rate of 200 mV s^{-1} for the flexible supercapacitor after cyclic mechanical deformation. (e) Optical image of a supercapacitor belt assembled using the CA-800 based flexible supercapacitor units, and (f) shows its schematic illustration.

flexible supercapacitor retained a stable capacitance output at various folding angles. Consistent with the CV measurements, the galvanostatic charge/discharge curves at different angles also display a similar nearly triangular shape, and the overall capacitance calculated by the discharge cycle decrease is less than 0.5% (Fig. 7c). Second, we carried out CV tests with sustained repeated bending operation utilizing a mold of a human wrist, and a schematic illustration of a single bending cycle is shown in Fig. S13.† After 10 000 bending cycles, strikingly, the CV curves still retain a similar rectangular shape (Fig. 7d),

reflecting the excellent capacitance output stability of the flexible supercapacitor for practical applications. Furthermore, the flexible supercapacitor can be easily extended to fabricate a new flexible integrated device, such as a supercapacitor belt (Fig. 7e and f).

In terms of the anode material of LIBs, carbon-based materials are still the most viable option for practical applications. Therefore, obtaining unique carbon nanostructures has aroused great interest in promoting the electrochemical performance. Here, we utilized a natural organism (kiwifruit) to
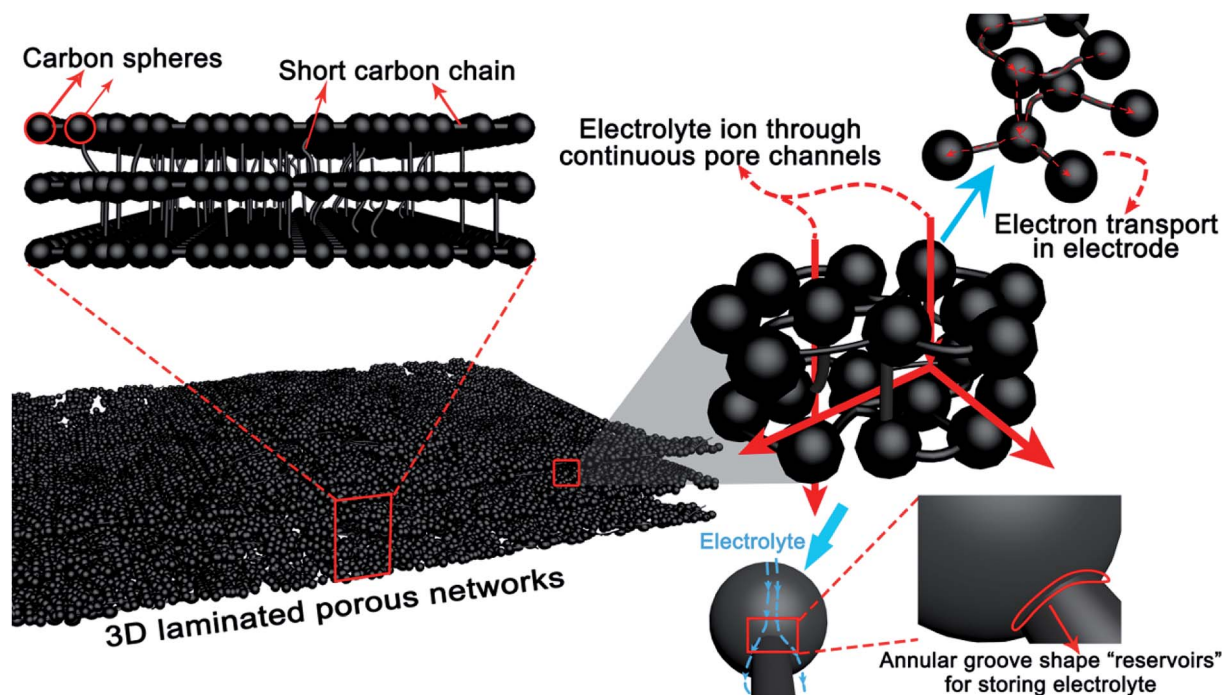
Fig. 8 Schematic illustration of the features of the 3D laminated structure for electrochemical energy storage.

synthesize porous carbon materials with a 3D laminated network constructed with short nano-chains bridging nanospheres. As illustrated in Fig. 8, the 3D network structure with continuous pore channels can facilitate efficient ionic diffusion, and the continuous carbon structure composed of nanospheres bridged with short nano-chains enables rapid electron transport in the electrode.[62] Meanwhile, the dual-carbon nanostructure can increase the interface between the active materials and the electrolyte to absorb the Li$^+$. The bridged regions between nanospheres and nano-chains can store electrolytes as annular groove shaped "reservoirs", thus shortening the diffusion distance of Li$^+$.[63] The unique three-dimensional bicontinuous structure is crucial for promoting the electrochemical performance. The ordered graphitic structure of a carbon material primarily determines the electron transport rate in an electrode. The heat-treatment temperature controls the porous structure and graphitization, and the CA-800 material is confirmed to possess optimized porosity and conductivity. As the electrode material for a supercapacitor, CA-800 achieves comparably high specific capacitances in aqueous and ionic liquid electrolytes. With the flake structure of the interconnected carbon spheres and short chains, the relatively large pores can provide a favorable path for transportation and penetration of ionic liquid electrolyte ions. Thus, the pore distribution of well-defined meso- and micropores is readily accessible to electrolyte ions because of the three-dimensional bicontinuous structure.

Conclusions

In summary, the low-temperature hydrothermal process retains the inherent nanofibers of kiwifruit and yields CAAs. Then, the conductive CAs with a 3D laminated porous network structure composed of short nano-chains bridging nanospheres were successfully prepared by a simple calcination. During the calcination process without a chemical activation agent, the balance of porosity and graphitization was controlled by the annealing temperature, and the best electrochemical performance for use in supercapacitors and as the anode of LIBs was achieved with the sample annealed at 800 °C. In addition, we engineered and assembled extensible, flexible and wearable supercapacitor devices, and the results of the two mechanical deformation tests confirm the stability of the capacitance output. It is interesting to explore biomass-derived carbon-based electrode materials with a consideration of utilizing and optimizing the natural structure of kiwifruit.

Experimental

The synthesis of CAs

The kiwifruit was first thoroughly washed and peeled. It was subsequently cut into the appropriate volume and then put into Teflon-lined stainless-steel autoclaves. Next, these autoclaves were directly placed into an oven and heated at 180 °C for 12 h. The resulting carbonaceous wet gel was immersed in deionized water and ethanol for several days to remove the soluble impurities. Subsequently, the wet gel was again immersed in pure deionized water to obtain the hydrogel. The corresponding CAAs were obtained by freeze drying these carbonaceous hydrogels. The electric porous CAs were prepared by calcining these pre-synthesized CAAs at 600 °C (CA-600), 800 °C (CA-800) and 1000 °C (CA-1000) for 2 h in a nitrogen atmosphere with a heating rate of 5 °C min^{-1}. As a control experiment, monodisperse carbon spheres (named RFCS-600) were synthesized using an extension of the Stöber method from Liu *et al.*[38]

Characterization

Field-emission SEM (Quanta FEG 250) and TEM (Tecnai G2 F20) were applied to look at the microstructure of the CAAs and CAs. X-ray powder diffraction was conducted using a Bruker D-8 Advance diffractometer with nickel-filtered Cu Kα (λ = 1.54178 Å) radiation at room temperature, and the data were collected from 5° to 75° with a scan rate of 2° min^{-1}. TGA was performed on a TG-209F1 (Netzsch) by heating the samples to 1000 °C at a rate of 5 °C min^{-1} in a nitrogen atmosphere. FTIR spectra (Nicolet iN10 MX) were used to determine the surface functional groups of these samples. XPS was conducted with two separate systems equipped with monochromatic Al Kα sources (ThermoFisher K-Alpha XPS system, USA) to analyze the chemical composition of the samples. EELS was carried out on a JEOL 2100-F TEM. Raman spectroscopy was performed using a multi-wavelength micro-Raman spectroscope (Renishaw RM2000) using 532 nm incident radiation and a 500× aperture. The measurements of the N_2 adsorption isotherms were done with a 3H-2000PM surface area and pore size analyzer (Beijing Beishide Instruments Co.) at 77.3 K to determine the surface areas of the CAs obtained at different annealing temperatures. The adsorption experiments with Ar (87.3 K) and CO_2 (273.2 K) were performed with a Micromeritics ASAP 2020 surface area and pore size analyzer (Micromeritics Instrument Ltd) to assess the surface area and pore characteristics. All samples were heated at 150 °C for 4 h under vacuum to remove all the adsorbed species. The specific surface area was determined by the Brunauer–Emmett–Teller (BET) method.

Electrochemical performances for LIBs

The samples were mixed with acetylene black and poly(vinylidene fluoride) (PVDF) at a weight ratio of 8 : 1 : 1 in N-methyl-2-pyrrolidone (NMP) to form the paste slurry. Subsequently, the resultant slurry was uniformly dispersed on a copper foil substrate. The obtained electrode sheet was dried in a vacuum oven at 120 °C for 12 h and then pressed. The electrolyte consisted of a solution of 1 M $LiPF_6$ in ethylene carbonate (EC)/dimethyl carbonate (DMC)/diethyl carbonate (DEC) (1 : 1 : 1, in wt%). CR2016-type coin cells were assembled in a glove box for electrochemical characterization. Lithium metal foil was used as both the counter and reference electrodes. The charge–discharge measurements were conducted using a cell testing instrument (LAND BTS 2013 A) over a potential range from 0.01 to 3.00 V. Cyclic voltammetry (CV) (0.01 V to 3.0 V, 0.1 mV s^{-1}) was performed using a CHI 660 E electrochemical workstation (Shanghai Chenhua Instruments Co.).

Electrochemical performances for supercapacitors

Electrochemical performance was evaluated using a CHI 660 E electrochemical workstation (Shanghai Chenhua Instruments Co.) using a three-electrode configuration in a 6 M KOH solution at room temperature. To prepare the working electrode, the paste slurry was first made by mixing the active-material (*i.e.*, CA-600, CA-800, and CA-1000), polytetrafluoroethylene (PTFE) and acetylene black with a weight ratio of 8 : 1 : 1 in absolute ethyl alcohol. The slurry was then rolled into a uniform thickness film with a mass loading of ~1.5 mg cm^{-2}, and it was dried in a vacuum oven at 80 °C for 12 h. The dried film was cut into the appropriate size (commonly, approximately 1 cm^2) and then pressed with an inactive nickel mesh current collector. Platinum gauze was used as the counter electrode, and a saturated calomel electrode as the reference electrode. CV measurements were conducted in the range of 0–1 V, and galvanostatic charge/discharge tests were conducted in the range of 0–1 V to avoid H_2O dissociation. EIS spectra were obtained in the frequency range from 10^5 Hz to 10^{-2} Hz at open circuit voltage with an alternate current amplitude of 5 mV. The cycle life tests were conducted by carrying out the galvanostatic charge/discharge measurements. The specific capacities (c) were calculated from the charge/discharge profiles based on eqn (1):

$$c = \frac{i\Delta t}{m\Delta v} \qquad (1)$$

where i, Δt, m and Δv are the discharge current (A), discharge time (s), active material mass (g) and potential change (V) within the discharge time.

The CA-800-based symmetric supercapacitor cell was fabricated as follows. The electrodes using CA-800 as the active material were prepared in a similar way to that described above. The coin cell (2025) was constructed by using two identical (weight and size) CA-800-based electrodes, an ion-porous separator (Celgard 3501) and BMIM BF_4 electrolyte. The gravimetric specific capacitance (C) for a single electrode was calculated according to eqn (2):

$$C = \frac{4I\Delta T}{M\Delta V} \qquad (2)$$

where I (A) is the current, ΔV (V) refers to the potential change within the discharge time ΔT (s), and M is the total mass (g) of active materials for both electrodes.

The CA-800-based extensible and flexible symmetric supercapacitor unit was assembled with copper conductive tape, a Celgard 2025 separator and BMIM BF_4 electrolyte. The pure active material was first stirred in absolute ethyl alcohol to make the slurry, and it was then spread on the flexible copper conductive tape with a mass loading of 4 mg cm^{-1}. The flexible electrodes were also dried in a vacuum oven at 50 °C for 12 h. These supercapacitor units were easily scalable through simple adhesion of the copper conductive tape.

Acknowledgements

Notes and references

1 B. Dunn, H. Kamath and J.-M. Tarascon, *Science*, 2011, **334**, 928–935.

2   X. Han, W.-M. Chen, X. Han, Y.-Z. Tan and D. Sun, *J. Mater. Chem. A*, 2016, **4**, 13040–13045.

3   Q. Chen, F. Lu, Y. Xia, H. Wang and X. Kuang, *J. Mater. Chem. A*, 2017, **5**, 4075–4083.

4   M. Winter and R. J. Brodd, *Chem. Rev.*, 2004, **104**, 4245–4270.

5   P. Simon and Y. Gogotsi, *Nat. Mater.*, 2008, **7**, 845–854.

6   Y. Wang, Y. Song and Y. Xia, *Chem. Soc. Rev.*, 2016, **45**, 5925–5950.

7   J. R. Miller and P. Simon, *Science Magazine*, 2008, **321**, 651–652.

8   Y. Deng, Y. Xie, K. Zou and X. Ji, *J. Mater. Chem. A*, 2016, **4**, 1144–1173.

9   L. Dong, C. Xu, Y. Li, Z.-H. Huang, F. Kang, Q.-H. Yang and X. Zhao, *J. Mater. Chem. A*, 2016, **4**, 4659–4685.

10 A. D. Roberts, X. Li and H. Zhang, *Chem. Soc. Rev.*, 2014, **43**, 4341–4356.

11 K. Gupta, T. Liu, R. Kavian, H. G. Chae, G. H. Ryu, Z. Lee, S. W. Lee and S. Kumar, *J. Mater. Chem. A*, 2016, **4**, 18294–18299.

12 M. Zeiger, N. Jäckel, V. N. Mochalin and V. Presser, *J. Mater. Chem. A*, 2016, **4**, 3172–3196.

13 P. Huang, M. Heon, D. Pech, M. Brunet, P.-L. Taberna, Y. Gogotsi, S. Lofland, J. D. Hettinger and P. Simon, *J. Power Sources*, 2013, **225**, 240–244.

14 Y. B. Yin, J. J. Xu, Q. C. Liu and X. B. Zhang, *Adv. Mater.*, 2016, **28**, 7494–7500.

15 L. Li, H. Yang, J. Yang, L. Zhang, J. Miao, Y. Zhang, C. Sun, W. Huang, X. Dong and B. Liu, *J. Mater. Chem. A*, 2016, **4**, 1319–1325.

16 G. Sun, X. Zhang, R. Lin, J. Yang, H. Zhang and P. Chen, *Angew. Chem., Int. Ed.*, 2015, **54**, 4651–4656.

17 J. Patiño, N. López-Salas, M. C. Gutiérrez, D. Carriazo, M. L. Ferrer and F. del Monte, *J. Mater. Chem. A*, 2016, **4**, 1251–1263.

18 M. Zou, Z. Ma, Q. Wang, Y. Yang, S. Wu, L. Yang, S. Hu, W. Xu, P. Han and R. Zou, *J. Mater. Chem. A*, 2016, **4**, 7398–7405.

19 M. Xie, X. Sun, H. Sun, T. Porcelli, S. M. George, Y. Zhou and J. Lian, *J. Mater. Chem. A*, 2016, **4**, 537–544.

20 H. Li, Y. Tao, X. Zheng, J. Luo, F. Kang, H.-M. Cheng and Q.-H. Yang, *Energy Environ. Sci.*, 2016, **9**, 3135–3142.

21 Y. Zuo, G. Wang, J. Peng, G. Li, Y. Ma, F. Yu, B. Dai, X. Guo and C.-P. Wong, *J. Mater. Chem. A*, 2016, **4**, 2453–2460.

22 J.-Y. Liu, X.-X. Li, J.-R. Huang, J.-J. Li, P. Zhou, J.-H. Liu and X.-J. Huang, *J. Mater. Chem. A*, 2017, **5**, 5977–5994.

23 M. M. Islam, C. M. Subramaniyam, T. Akhter, S. N. Faisal, A. I. Minett, H. K. Liu, K. Konstantinov and S. X. Dou, *J. Mater. Chem. A*, 2017, **5**, 5290–5302.

24 Y.-H. Huang, Q. Bao, J.-G. Duh and C.-T. Chang, *J. Mater. Chem. A*, 2016, **4**, 9986–9997.

25 Z. Lei, J. Zhang, L. L. Zhang, N. A. Kumar and X. Zhao, *Energy Environ. Sci.*, 2016, **9**, 1891–1930.

26 G. Zhang, S. Hou, H. Zhang, W. Zeng, F. Yan, C. C. Li and H. Duan, *Adv. Mater.*, 2015, **27**, 2400–2405.

27 J. Wang, P. Nie, B. Ding, S. Dong, X. Hao, H. Dou and X. Zhang, *J. Mater. Chem. A*, 2017, **5**, 2411–2428.

28 Y. Li, Y.-S. Hu, H. Li, L. Chen and X. Huang, *J. Mater. Chem. A*, 2016, **4**, 96–104.

29 D. Xie, X.-H. Xia, W.-J. Tang, Y. Zhong, Y.-D. Wang, D.-H. Wang, X.-L. Wang and J.-P. Tu, *J. Mater. Chem. A*, 2017, **5**, 7578–7585.

30 J. Hou, C. Cao, F. Idrees and X. Ma, *ACS Nano*, 2015, **9**, 2556–2564.

31 E. Hao, W. Liu, S. Liu, Y. Zhang, H. Wang, S. Chen, F. Cheng, S. Zhao and H. Yang, *J. Mater. Chem. A*, 2017, **5**, 2204–2214.

32 K. Xiao, L.-X. Ding, H. Chen, S. Wang, X. Lu and H. Wang, *J. Mater. Chem. A*, 2016, **4**, 372–378.

33 J. Cui, Y. Xi, S. Chen, D. Li, X. She, J. Sun, W. Han, D. Yang and S. Guo, *Adv. Funct. Mater.*, 2016, **26**, 8487–8495.

34 Q. Wang, J. Yan and Z. Fan, *Energy Environ. Sci.*, 2016, **9**, 729–762.

35 A. Jain, R. Balasubramanian and M. Srinivasan, *Chem. Eng. J.*, 2016, **283**, 789–805.

36 B. Hu, K. Wang, L. Wu, S. H. Yu, M. Antonietti and M. M. Titirici, *Adv. Mater.*, 2010, **22**, 813–828.

37 M.-M. Titirici, R. J. White, N. Brun, V. L. Budarin, D. S. Su, F. del Monte, J. H. Clark and M. J. MacLachlan, *Chem. Soc. Rev.*, 2015, **44**, 250–290.

38 J. Liu, S. Z. Qiao, H. Liu, J. Chen, A. Orpe, D. Zhao and G. Q. M. Lu, *Angew. Chem., Int. Ed.*, 2011, **50**, 5947–5951.

39 Y. Zhu, S. Murali, M. D. Stoller, K. J. Ganesh, W. Cai, P. J. Ferreira, A. Pirkle, R. M. Wallace, K. A. Cychosz, M. Thommes, D. Su, E. A. Stach and R. S. Ruoff, *Science*, 2011, **332**, 1537–1541.

40 J. P. Paraknowitsch, J. Zhang, D. Su, A. Thomas and M. Antonietti, *Adv. Mater.*, 2010, **22**, 87–92.

41 C. Casiraghi, A. Hartschuh, H. Qian, S. Piscanec, C. Georgi, A. Fasoli, K. Novoselov, D. Basko and A. Ferrari, *Nano Lett.*, 2009, **9**, 1433–1441.

42 M. Thommes, K. Kaneko, A. V. Neimark, J. P. Olivier, F. Rodriguez-Reinoso, J. Rouquerol and K. S. Sing, *Pure Appl. Chem.*, 2015, **87**, 1051–1069.

43 G. Tan, F. Wu, Y. Yuan, R. Chen, T. Zhao, Y. Yao, J. Qian, J. Liu, Y. Ye and R. Shahbazian-Yassar, *Nat. Commun.*, 2016, **7**, 11774.

44 J. Maier, *Nat. Mater.*, 2005, **4**, 805–815.

45 Q. Xu, J. Y. Li, J. K. Sun, Y. X. Yin, L. J. Wan and Y. G. Guo, *Adv. Energy Mater.*, 2017, **7**, 1601481.

46 L. Qie, W. M. Chen, Z. H. Wang, Q. G. Shao, X. Li, L. X. Yuan, X. L. Hu, W. X. Zhang and Y. H. Huang, *Adv. Mater.*, 2012, **24**, 2047–2050.

47 R. R. Gaddam, D. Yang, R. Narayan, K. Raju, N. A. Kumar and X. Zhao, *Nano Energy*, 2016, **26**, 346–352.

48 G. Xu, J. Han, B. Ding, P. Nie, J. Pan, H. Dou, H. Li and X. Zhang, *Green Chem.*, 2015, **17**, 1668–1674.

49 J. Ou, Y. Zhang, L. Chen, Q. Zhao, Y. Meng, Y. Guo and D. Xiao, *J. Mater. Chem. A*, 2015, **3**, 6534–6541.

50 W. Lv, F. Wen, J. Xiang, J. Zhao, L. Li, L. Wang, Z. Liu and Y. Tian, *Electrochim. Acta*, 2015, **176**, 533–541.

51 B. Campbell, R. Ionescu, Z. Favors, C. S. Ozkan and M. Ozkan, *Sci. Rep.*, 2015, **5**, 14575.

52 X. Zhou, F. Chen, T. Bai, B. Long, Q. Liao, Y. Ren and J. Yang, *Green Chem.*, 2016, **18**, 2078–2088.

53 K. Saravanan and N. Kalaiselvi, *Carbon*, 2015, **81**, 43–53.

54 H. Ru, K. Xiang, W. Zhou, Y. Zhu, X. S. Zhao and H. Chen, *Electrochim. Acta*, 2016, **222**, 551–560.

55 W. Tian, Q. Gao, Y. Tan, K. Yang, L. Zhu, C. Yang and H. Zhang, *J. Mater. Chem. A*, 2015, **3**, 5656–5664.

56 G. Ma, Q. Yang, K. Sun, H. Peng, F. Ran, X. Zhao and Z. Lei, *Bioresour. Technol.*, 2015, **197**, 137–142.

57 H. Chen, D. Liu, Z. Shen, B. Bao, S. Zhao and L. Wu, *Electrochim. Acta*, 2015, **180**, 241–251.

58 S. Song, F. Ma, G. Wu, D. Ma, W. Geng and J. Wan, *J. Mater. Chem. A*, 2015, **3**, 18154–18162.

59 Y. Huang, J. He, Y. Luan, Y. Jiang, S. Guo, X. Zhang, C. Tian and B. Jiang, *RSC Adv.*, 2017, **7**, 10385–10390.

60 Z. Ling, Z. Wang, M. Zhang, C. Yu, G. Wang, Y. Dong, S. Liu, Y. Wang and J. Qiu, *Adv. Funct. Mater.*, 2016, **26**, 111–119.

61 M. Genovese and K. Lian, *J. Mater. Chem. A*, 2017, **5**, 3939–3947.

62 H. Zhang, X. Yu and P. V. Braun, *Nat. Nanotechnol.*, 2011, **6**, 277–281.

63 M. Shi, T. Wu, X. Song, J. Liu, L. Zhao, P. Zhang and L. Gao, *J. Mater. Chem. A*, 2016, **4**, 10666–10672.